

# Numerical study of transitions in lid-driven flows in semicircular cavities

Tsorng-Whay Pan<sup>a,1</sup>, Ang Li<sup>b</sup>, and Shang-Huan Chiu<sup>c</sup>

<sup>a</sup> Department of Mathematics, University of Houston, Houston, Texas 77204, USA

<sup>b</sup> Department of Mathematics, Lane College, Jackson, TN 38301, USA

<sup>c</sup> Department of Mathematics, Lehigh University, Bethlehem, PA, 18015, USA

**Abstract** In this article, three-dimensional (3D) lid-driven flows in semicircular cavities are studied. The numerical solution of the Navier-Stokes equations modeling incompressible viscous fluid flow in cavities is obtained via a methodology combining a first-order accurate operator-splitting scheme, a fictitious domain formulation, and finite element space approximations. The critical Reynolds numbers ( $Re_{cr}$ ) for having oscillatory flow (a Hopf bifurcation) are obtained. The associated oscillating motion in a semicircular cavity with length equal to width has been studied in detail. Based on the averaged velocity field in one period of oscillating motion, the flow difference (called oscillation mode) between the velocity field and averaged one at several time instances in such period shows almost the same flow pattern for the Reynolds numbers close to  $Re_{cr}$ . This oscillation mode in a semicircular cavity shows a close similarity to the one obtained in a shallow cavity, but with some difference in a shallow cavity which is triggered by the presence of two vertical side walls and downstream wall.

**Keywords** Lid driven cavity flow, semicircular cavities, Taylor-Görtler-like vortices, Hopf bifurcation, projection method.

## 1 Introduction

Lid-driven cavity flow is a classical benchmark flow problem for validating numerical methods and comparing results obtained from laboratory and computational experiments due to its geometrical simplicity and unambiguous boundary conditions (e.g., see [2], [3], and [4]). This flow problem is important to the basic study of fluid mechanics, including boundary layers,

---

<sup>1</sup>Corresponding author: e-mail: tpan@uh.edu

primary vortex, secondary flows (such as the corner vortices and Taylor-Goertler-like vortices), various instabilities and transitions, and turbulence; this flow system is also relevant to many industrial applications (e.g., see [2] and [5]). Most lid-driven cavity flows were studied in two-dimensional (2D) and three-dimensional (3D) rectangular cavities; but, e.g., some other shapes like those with triangular, polar or sectorial cross section were also considered (see a review article [4] for some of those non-rectangular cases). For cavities with a circular shape boundary, there are fewer results available (compared to rectangular cavities) as pointed out in [4] and [6]. In [7] and [8], lid-driven cavity flows have been obtained in a hemispherical cavity and its transition has been studied in [8]. In [9], a spectral element discretization was developed to solve lid-driven flows in a full disk with a moving circular lid. A similar one was also considered later in [6], and a circular cavity with an horizontal top boundary was also studied in [6]. Although two-dimensional flows were obtained in [6], their 3D linear stability analyses were done and confirmed by spectral direct numerical simulations with periodic flows in the spanwise direction. In a 2D semicircular cavity, a classic finite element approach was used to solve lid-driven flows in [10]. Such method has shown no difficulty at capturing the formation of primary, secondary and tertiary vortices as  $Re$  increases; it also has the capability in capturing the transition from steady flow to oscillatory flow (a Hopf bifurcation phenomenon). In [11], a 3D semicircular cavity was one of several cavity shapes used to study experimentally the shape influence on the birth and evolution of recirculating flow structures in cavities. The evolution of lid-driven flow in a semicircular cavity was studied up to the dimensionless time  $t=12$  since semicircular flow seems to reach its steady state as claimed in [11] and flow transition to oscillatory one was not mentioned.

It is known that, depending on the solution method, boundary conditions and mesh size used in simulation, the critical Reynolds number ( $Re_{cr}$ ) for the occurrence of transition from steady flow to oscillatory flow varies in cavities. For example, Iwatsu *et al.* [12] obtained numerically a pair of Taylor-Görtler-like vortices for a cubic lid-driven cavity flow at  $Re=2000$ . Giannetti *et al.* [13] also obtained that the cubic lid-driven cavity flow becomes unstable for  $Re$  just above 2000 via the three-dimensional global linear stability analysis. Feldman and Gelfgat [14] obtained the critical Reynolds number for transition occurring at  $Re_{cr} = 1914$ . Liberzon *et al.* [15] experimentally obtained the critical Reynolds number is in the range [1700, 1970]. In [16], Pan *et al.* found the critical Reynolds number value is between 1894

and 1895 for lid-driven flows in a cube. In this article, we have studied numerically the transition from steady flow to oscillatory one in semicircular cavities. We have applied a first-order accurate operator-splitting scheme, the Lie scheme (e.g., see [8] and [17] for its details), with a fictitious domain approach and finite element method to obtain numerical solutions of the Navier-Stokes equations. This numerical methodology is an extension of the investigations reported in [18] and [19]. The resulting methodology is easy to implement and quite modular since, at each time step, one has to solve a sequence of four simpler sub-problems. To investigate the mode associated with the transition from steady flow to oscillatory flow, we have focused on the flow fields at Reynolds numbers close to  $Re_{cr}$ . The difference of flow field with respect to the averaged flow field in one period of the oscillation has been studied and compared with those that occurred in a shallow cavity with unit square base. The outline of this paper is as follows: We first introduce the formulation of the flow problem and then the numerical method briefly in Section 2. In Section 3, numerical results obtained for lid-driven flows in semicircular cavities are presented. Then the transition from steady flow to oscillatory flow has been studied, especially on the comparison of oscillatory modes in two different cavities. Conclusions are summarized in Section 4.

## 2 Problem formulation

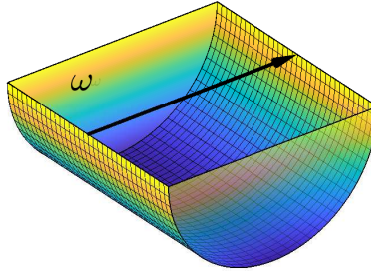


Figure 1: An example of a semicircular cavity  $\omega$ .

The governing equations for modeling incompressible viscous Newtonian fluid flow in a cavity  $\omega \subset \mathbb{R}^3$  (see Figure 1) for  $T > 0$  are the Navier-Stokes

equations, namely

$$\begin{aligned}
(1) \quad & \frac{\partial \mathbf{u}}{\partial t} - \nu \Delta \mathbf{u} + (\mathbf{u} \cdot \nabla) \mathbf{u} + \nabla p = \mathbf{0} \quad \text{in } \omega \times (0, T), \\
(2) \quad & \nabla \cdot \mathbf{u} = 0 \quad \text{in } \omega \times (0, T), \\
(3) \quad & \mathbf{u}(0) = \mathbf{u}_0, \quad \text{with } \nabla \cdot \mathbf{u}_0 = 0, \\
(4) \quad & \mathbf{u} = \mathbf{u}_B(\mathbf{x}) \quad \text{on } \partial\omega \times (0, T) \quad \text{with } \int_{\partial\omega} \mathbf{u}_B \cdot \mathbf{n} d\gamma = 0 \quad \text{on } (0, T),
\end{aligned}$$

where  $\mathbf{u}$  and  $p$  are the flow velocity and pressure, respectively,  $\nu$  is a viscosity coefficient, and  $\mathbf{n}$  is the unit outward normal vector at the boundary  $\gamma = \partial\omega$ . For lid-driven flows considered in this article, the boundary data  $\mathbf{u}_B(\mathbf{x})$  is  $(1, 0, 0)^t$  on the top moving lid and zero elsewhere on the boundary of  $\omega$ . We denote by  $v(t)$  the function  $\mathbf{x} \rightarrow v(\mathbf{x}, t)$ ,  $\mathbf{x}$  being the generic point of  $\mathbb{R}^3$ .

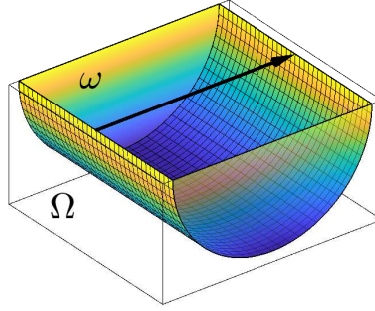


Figure 2: An example of a semicircular cavity  $\omega$  embedded into a simple shape fictitious domain  $\Omega$ .

To solve problem (1)-(4) numerically, we have first embedded the fluid flow domain  $\omega$  into a larger simple shape domain  $\Omega$  (so-called fictitious domain, see Figure 2) and obtained its fictitious domain formulation

$$\begin{aligned}
(5) \quad & \frac{\partial \mathbf{U}}{\partial t} - \nu \Delta \mathbf{U} + (\mathbf{U} \cdot \nabla) \mathbf{U} + \nabla P = \boldsymbol{\lambda} \quad \text{in } \Omega \times (0, T), \\
(6) \quad & \nabla \cdot \mathbf{U} = 0 \quad \text{in } \Omega \times (0, T), \\
(7) \quad & \mathbf{U}(0) = \mathbf{U}_0, \quad \text{with } \nabla \cdot \mathbf{U}_0 = 0, \\
(8) \quad & \mathbf{U} = \mathbf{U}_B(\mathbf{x}) \quad \text{on } \partial\Omega \times (0, T) \quad \text{with } \int_{\partial\Omega} \mathbf{U}_B \cdot \mathbf{n} d\gamma = 0 \quad \text{on } (0, T), \\
(9) \quad & \mathbf{U} = \mathbf{0} \quad \text{in } \Omega \setminus \bar{\omega} \times (0, T),
\end{aligned}$$

where  $\boldsymbol{\lambda}$  is a distributed Lagrange multiplier, which vanishes in  $\omega$ , and acts as a pseudo body force so that  $\mathbf{U} = \mathbf{0}$  is enforced in  $\Omega \setminus \bar{\omega}$ ,  $\mathbf{U}_0|_{\omega} = \mathbf{u}_0$ , and  $\mathbf{U}_B$  is  $(1, 0, 0)^t$  on the top moving lid of  $\omega$  and zero elsewhere on the boundary of  $\Omega$ . Actually, the above distributed Lagrange multiplier approach has been successfully applied to simulate the motion of particles freely moving in a fluid (see, e.g., [20], [21], [22]). Then via the Lie scheme (see, e.g., see [8] and [17] for the details) to obtain the numerical solution of lid-driven flow problem, we have time-discretized problem (5)-(9) into a sequence of four sub-problems for each time step, namely: (i) using a  $L^2$ -projection Stokes solver à la Uzawa to force the incompressibility condition, (ii) an advection step, (iii) a diffusion step, and (iv) enforcement zero velocity outside the cavity  $\omega$ . A similar one for simulating lid-driven flow in a hemispherical cavity can be found in [8] (Ch. 7). Lie scheme is first-order accurate in time, but its low order time accuracy is compensated by its modularity, easy implementation, stability, and robustness properties. The first three steps were used to obtain numerical results of lid-driven flow in shallow cavities reported in [16].

For the space discretization, we have used, as in [23] (Chapter 5) and [24], a  $P_1$ -*iso*- $P_2$  (resp.,  $P_1$ ) finite element approximation for the velocity field (resp., pressure) defined on uniform “tetrahedral” meshes  $\mathcal{T}_h$  (resp.,  $\mathcal{T}_{2h}$ ) due to the simple shape of fictitious domain. The resulting four sub-problems via the Lie scheme are very classical problems and each one of them can be solved by a variety of existing methods, this being one of the key points of the operator-splitting methodology. For the first one, an  $L^2$ -projection (equivalent to a saddle-point problem), it can be solved by an Uzawa/preconditioned conjugate gradient algorithm as discussed in [23] (Section 21). The advection problem at the second step is solved by a wave-like equation method (see, e.g., [25], [26], and [8] (Ch. 3)) which is explicit and does not introduce numerical dissipation. Since the advection problem is decoupled from the others, a sub-time step satisfying the CFL condition can be chosen easily. A classical elliptic problem at the third step can be solved easily. The last one is also a saddle-point problem, which is solved by a conjugate gradient algorithm as discussed in, e.g., [8] (Ch. 7).

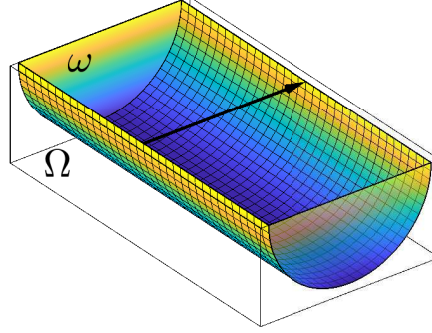


Figure 3: A semicircular cavity  $\omega$  of width 2, depth 1, and height 0.5 (embedded into a fictitious domain  $\Omega$ ) where the radius of circular sector is 0.5.

### 3 Numerical Results and discussions

For the first semicircular cavity shown in Figure 3, we have taken  $\Omega = (-2h, 1 + 2h) \times (0, 2) \times (-2h, 0.5)$  as a computational domain (fictitious domain) where  $h$  is the mesh size for the velocity field and the radius of circular sector is 0.5 and defined the Dirichlet data  $\mathbf{U}_B$  by

$$\mathbf{U}_B(\mathbf{x}) = \begin{cases} (1, 0, 0)^T & \text{on } \{\mathbf{x} \mid \mathbf{x} = (x_1, x_2, 0.5)^T, 0 < x_1 < 1, 0 < x_2 < 2\}, \\ \mathbf{0} & \text{elsewhere on } \partial\Omega, \end{cases}$$

Then the Reynolds number is  $\text{Re}=1/\nu$ . We assumed that a steady state has been reached when the change between two consecutive time steps,  $\|\mathbf{U}_h^n - \mathbf{U}_h^{n-1}\|_\infty / \Delta t$ , in the simulation is less than  $10^{-7}$ , and then took  $\mathbf{U}_h^n$  as the steady state solution. This semicircular cavity was one of several cavity shapes used in [11] to study the shape influence on birth and evolution of recirculating flow structures in cavities. The Reynolds number for the experiment considered in [11] is  $\text{Re}=1000$ . To validate the numerical methodologies briefly described in the previous section, we have obtained the initial phase of the flow establishment with the velocity mesh size  $h = 1/96$  and time step  $\Delta t=0.001$ . For the star-up flow, numerical results were computed for the first 9 seconds (see Figure 4). In Figure. 5, the vortex-core trajectory of numerical results on the middle vertical plane  $x_2 = 1$  shows a very good agreement with those obtained in [11]. Our numerical results suggest that

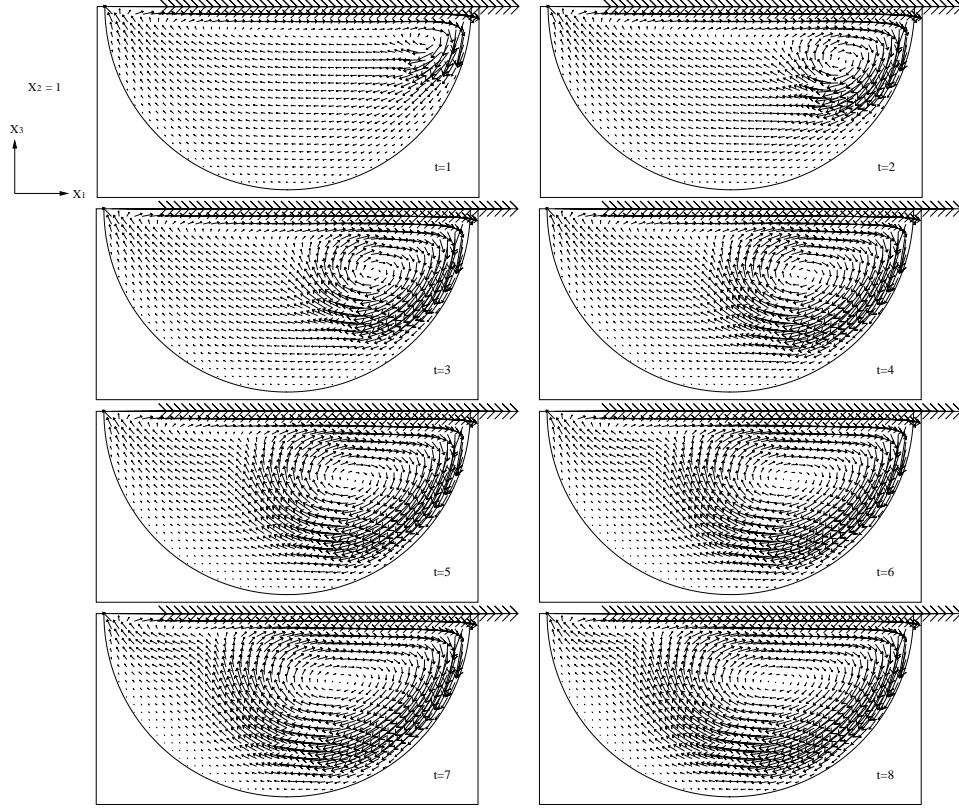


Figure 4: Projected velocity vectors on the plane  $x_2 = 1$  at different times for  $Re=1000$ .

the critical Reynolds number for the transition from steady state flow to oscillatory one is close to  $Re=790$ . The critical Reynolds number suggested in [11] is higher than 1000 since they believed that the lid-driven flow in a semicircular cavity reported in [11] is steady for  $Re=1000$ .

To investigate the effect of semicircular shape on the transition of lid-driven cavity flows, we have considered the second semicircular cavity as shown in Figure 6. Its radius of circular sector is 0.5 and fictitious domain is  $\Omega = (-2h, 1+2h) \times (0, 1) \times (-2h, 0.5)$ . The Dirichlet data  $\mathbf{U}_B$  is defined as

$$(11) \quad \mathbf{U}_B(\mathbf{x}) = \begin{cases} (1, 0, 0)^T & \text{on } \{\mathbf{x} \mid \mathbf{x} = (x_1, x_2, 0.5)^T, 0 < x_1, x_2 < 1\}, \\ \mathbf{0} & \text{elsewhere on } \partial\Omega, \end{cases}$$



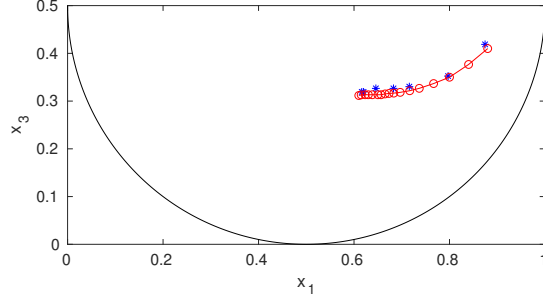


Figure 5: Primary vortex-core trajectory in a semicircular cavity for  $Re=1000$ : Experimental data (\*) taken from [11] and numerical results for  $1 \leq t \leq 9$  sec (red solid line with  $\circ$ 's).

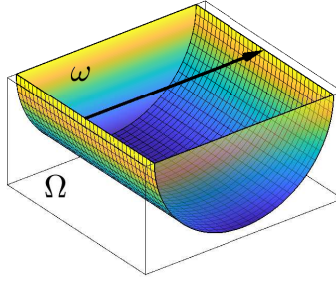


Figure 6: A semicircular cavity  $\omega$  of width 1, depth 1, and height 0.5 (embedded into a fictitious domain  $\Omega$ ) where the radius of circular sector is 0.5.

We like to compare the resulting flows in this semicircular cavity with those in a shallow cavity with a unit square base and height 0.5 discussed in [16].

The steady flow velocity vectors for  $Re=400$  and  $900$  are shown in Figures 7 and 8, respectively where the velocity field vectors for  $Re=400$  (resp.,  $Re=900$ ) are projected onto the three planes,  $x_2 = 0.5$ ,  $x_1 = 63/96$ , and  $x_3 = 0.3125$  (resp.,  $x_2 = 0.5$ ,  $x_1 = 54/96$ , and  $x_3 = 0.3125$ ). The length of vectors has been enlarged two times in the two planes,  $x_1 = 54/96$  and  $x_3 = 0.3125$ , to improve clarity. The two plots on  $x_2 = 0.5$  show that the center of primary vortex moves toward the central region as  $Re$  increases from 400 to 900. At  $Re=400$ , on  $x_1 = 63/96$ , there is a vortex occurring close to each bottom corner but another pair of vortices is shown in the central region on  $x_1 = 54/96$  for  $Re=900$ . Similarly, four established vortices appear



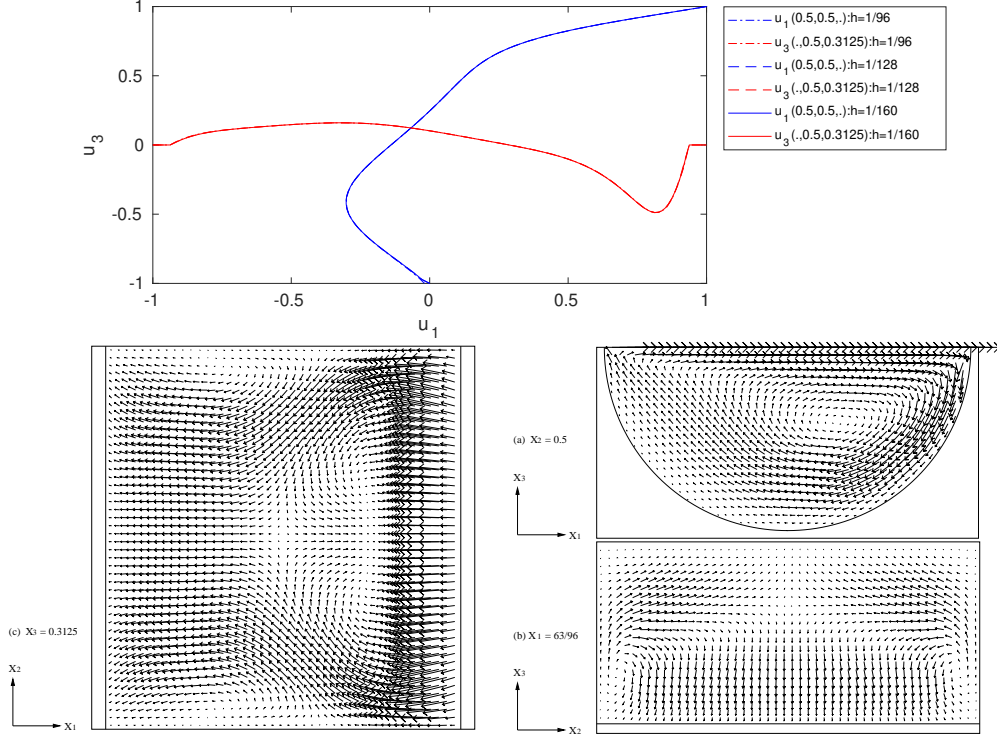


Figure 7: (i)  $Re=400$ : Comparisons of the numerical results obtained for  $h = 1/96, 1/128$ , and  $1/160$  (top), (ii) Steady flow velocity vector projected on planes:  $x_3 = 0.3125$  (bottom left),  $x_2 = 0.5$  (middle right), and  $x_1 = 63/96$  (bottom right) for  $h = 1/96$  and  $\Delta t=0.001$ . (In the bottom left and right plots, vector scale is two times of the actual one to enhance visibility.)

on  $x_3 = 0.3125$  for  $Re=900$ ; but not for  $Re=400$ .

For lid-driven flows in a cavity, one of many interesting questions is to locate the critical Reynolds number  $Re_{cr}$  for a transition from a steady lid-driven flow to oscillatory one. In, e.g., [14] and [15],  $Re_{cr}$  was predicted to be less than 2000 for lid-driven flows in a cubic cavity. On the other hand, Gianetti *et al.* found (ref. [13]) that the cubic lid-driven cavity flow becomes unstable for  $Re$  just above 2000 via a global linear stability analysis. Kuhlmann and Altensoeder [27] obtained numerically that the critical Reynolds number value is 1919.51. In [16], Pan *et al.* found the critical Reynolds number value is between 1894 and 1895 in a cubic cavity. These results indicate that the Hopf bifurcation related to the oscillating flows oc-

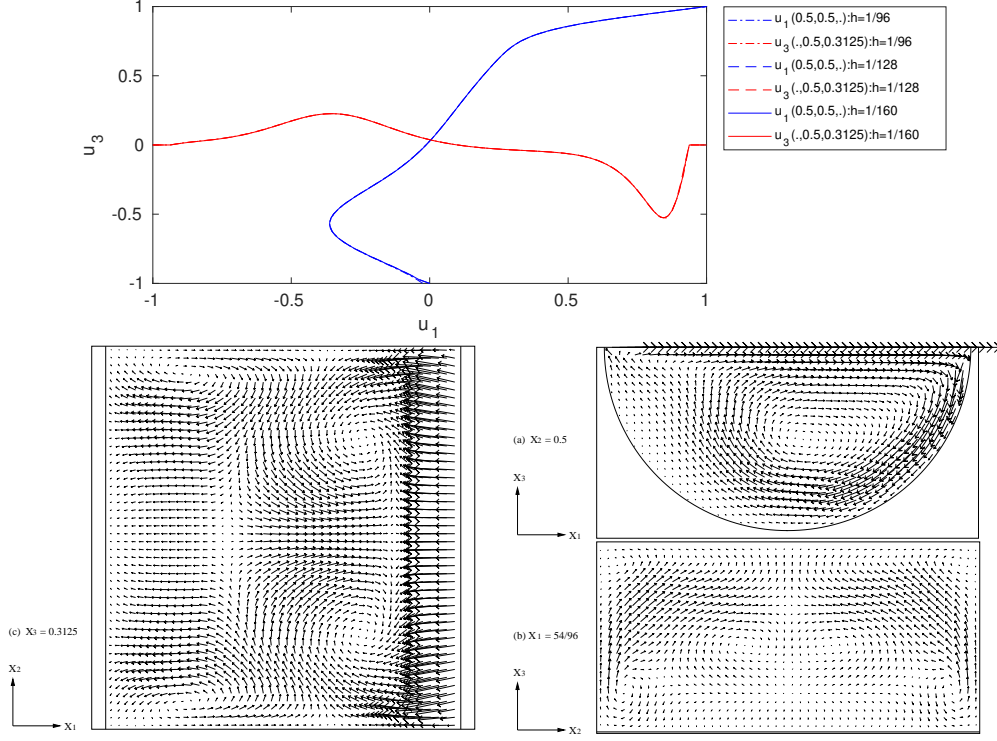


Figure 8: (i)  $Re=900$ : Comparisons of the numerical results obtained for  $h = 1/96, 1/128$ , and  $1/160$  (top), (ii) Steady flow velocity vector projected on planes:  $x_3 = 0.3125$  (bottom left),  $x_2 = 0.5$  (middle right), and  $x_1 = 54/96$  (bottom right) for  $h = 1/96$  and  $\Delta t=0.001$ . (In the bottom left and right plots, vector scale is two times of the actual one to enhance visibility.)

curs for  $Re$  slightly below 2000 for lid-driven flows in a cubic cavity. To study the effect of cavity shape on the transition of lid-driven flows, we first like to locate the value of  $Re_{cr}$  for lid-driven flows in a semicircular cavity (see Figure 6) and then study the oscillation flows for the Reynolds numbers close to  $Re_{cr}$ . We have computed the flow velocity  $\mathbf{u}_h^n$  for different  $Re$  values and mesh sizes  $h$  and analyzed its history of  $L^2$ -norm (i.e., plot of  $\|\mathbf{u}_h^n\|$  versus  $t$ ). For  $h = 1/96$  and  $\Delta t=0.001$ , the flow field evolves to a steady state and the amplitude of its  $L^2$ -norm oscillation decreases in time for  $Re \leq 927$  (see Figure 9). For  $Re \geq 928$ , the steady state criterion is not satisfied and the amplitude of oscillation increases in time (see Figure 9). Thus we conclude that the critical Reynolds number  $Re_{cr}$  for the occurrence of tran-

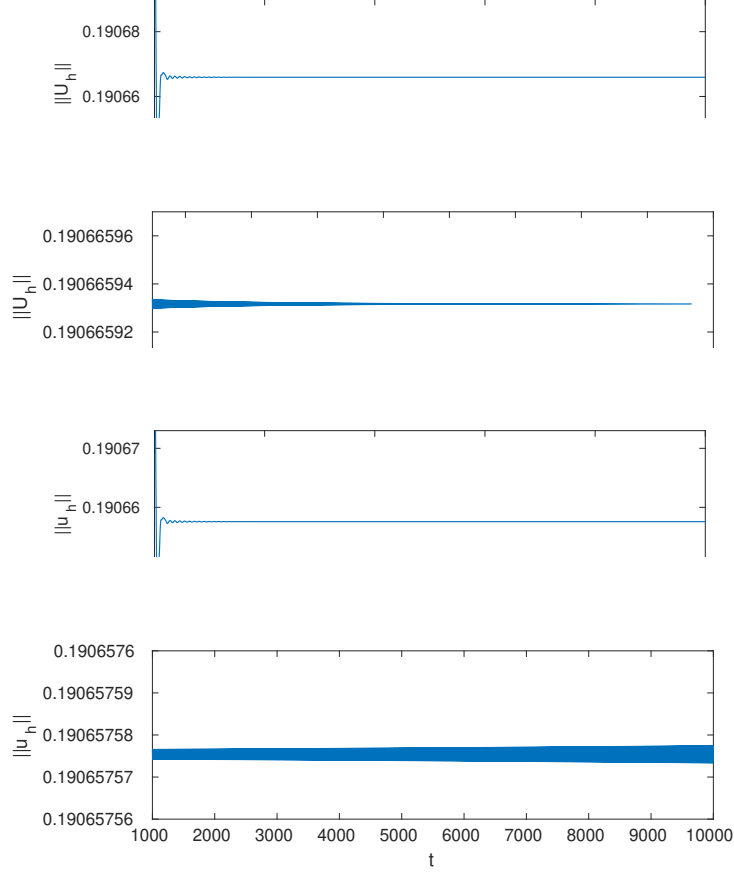


Figure 9: Histories of  $\|\mathbf{u}_h\|$  for  $Re = 927$  (top two) and  $928$  (bottom two) obtained with  $h = 1/96$  and  $\Delta t = 0.001$ .

sition is somewhere between 927 and 928. The oscillating angular frequency is between 0.70376 and 0.70345. Applying the same analysis to the histories of flow velocity  $L^2$ -norm for  $h = 1/160$  and  $\Delta t = 0.001$ , the critical  $Re_{cr}$  is between 934 and 935. The oscillating angular frequency is between 0.70645 and 0.70629.

Concerning the oscillation shown in the history of  $L^2$ -norm  $\|\mathbf{u}_h^n\|$ , we have first computed the averaged velocity field from those obtained at different time instances denoted by “\*” in one period as shown in the top plot of Figure 10 for  $Re=927$ . Then we look into the change of velocity field by comparing it to the average one obtained in the same period. The difference

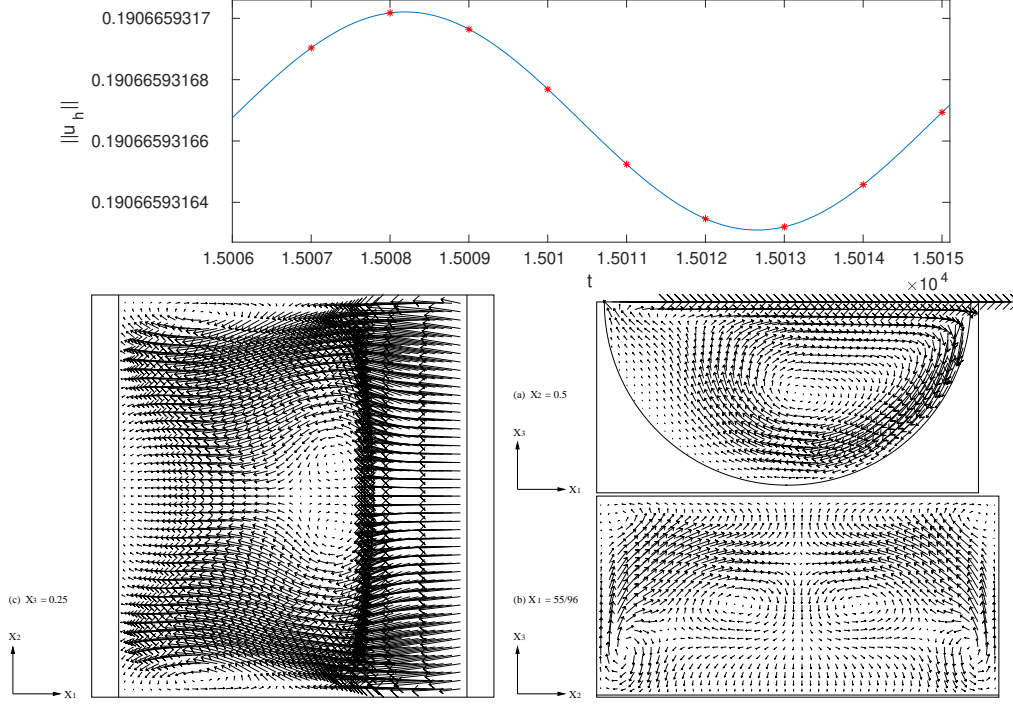


Figure 10: History of  $\|u_h\|$  for one period in a semicircular cavity for  $Re = 927$  (top), averaged velocity field projected one planes:  $x_3 = 0.25$  (bottom left),  $x_2 = 0.5$  (middle right), and  $x_1 = 55/96$  (bottom right) for  $h = 1/96$  and  $\Delta t = 0.001$ . (In the bottom left and right plots, the vector scale is four times that of the actual one to enhance visibility.)

between averaged velocity field and the one at four time instances in the same time period are shown in Figure 11 for  $Re=927$ . The flow direction of the difference of velocity field projected on plane  $x_2 = 55/96$  at  $t = 15008$  (resp.,  $t = 15010.5$ ) is opposed to the one at  $t = 15012.5$  (resp.,  $t = 15015$ ), but the flow circulation pattern is almost the same. Similar behavior of flow direction and pattern are also found for the projection on plane  $x_3 = 0.25$  in Figure 11. Since the difference between velocity field and the average one is a kind of “oscillation mode” (as shown in Figure 11), we shall look into the difference of velocity field obtained from the first half of the period in following discussion. Even though the oscillating amplitude for  $Re=927$  decreases in time, the same oscillation mode has been obtained for  $Re=928$

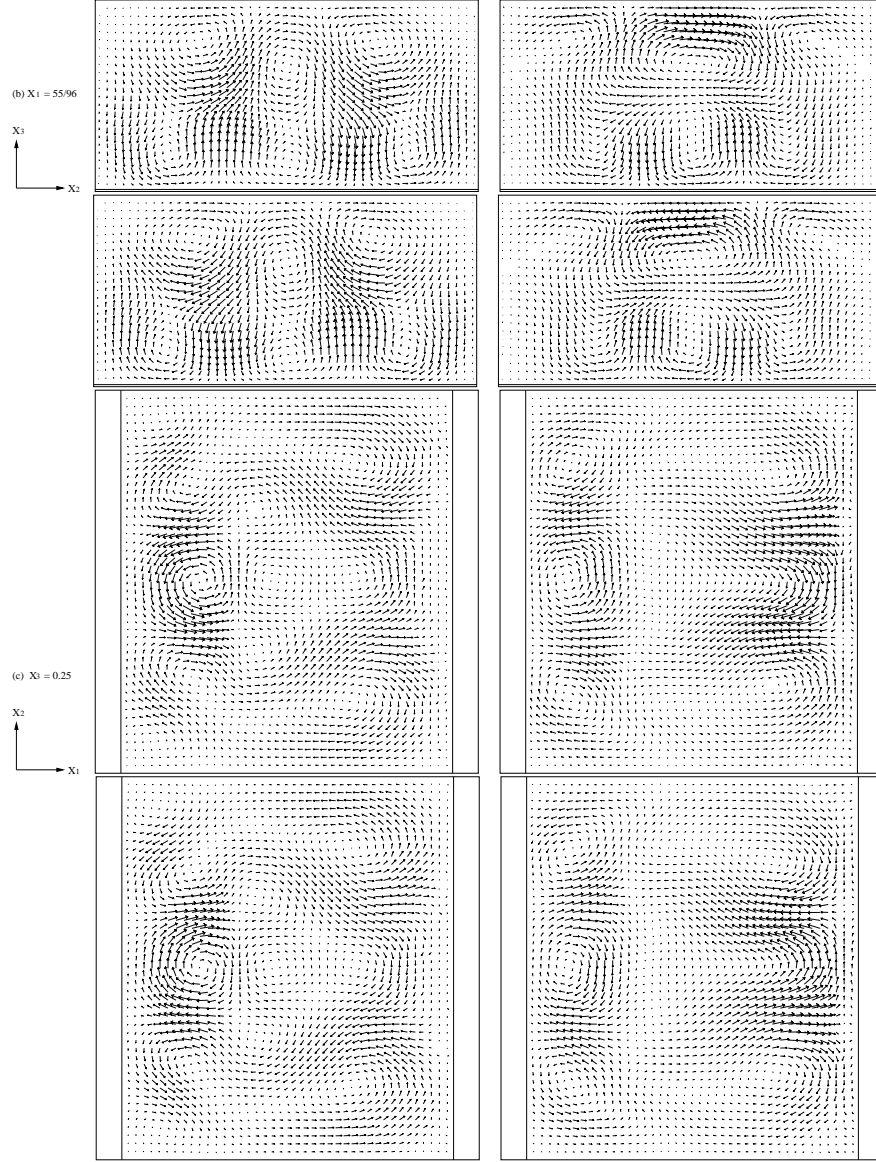


Figure 11: Velocity field oscillation (difference) projecting on the planes  $x_1 = 55/96$  (top four) and  $x_3 = 0.25$  (bottom four) at  $t = 15008, 15010.5, 15012.5$ , and  $15015$  (from left to right and then from top to bottom) for  $Re=927$ . The velocity vectors have been magnified in those plots to enhance visibility.

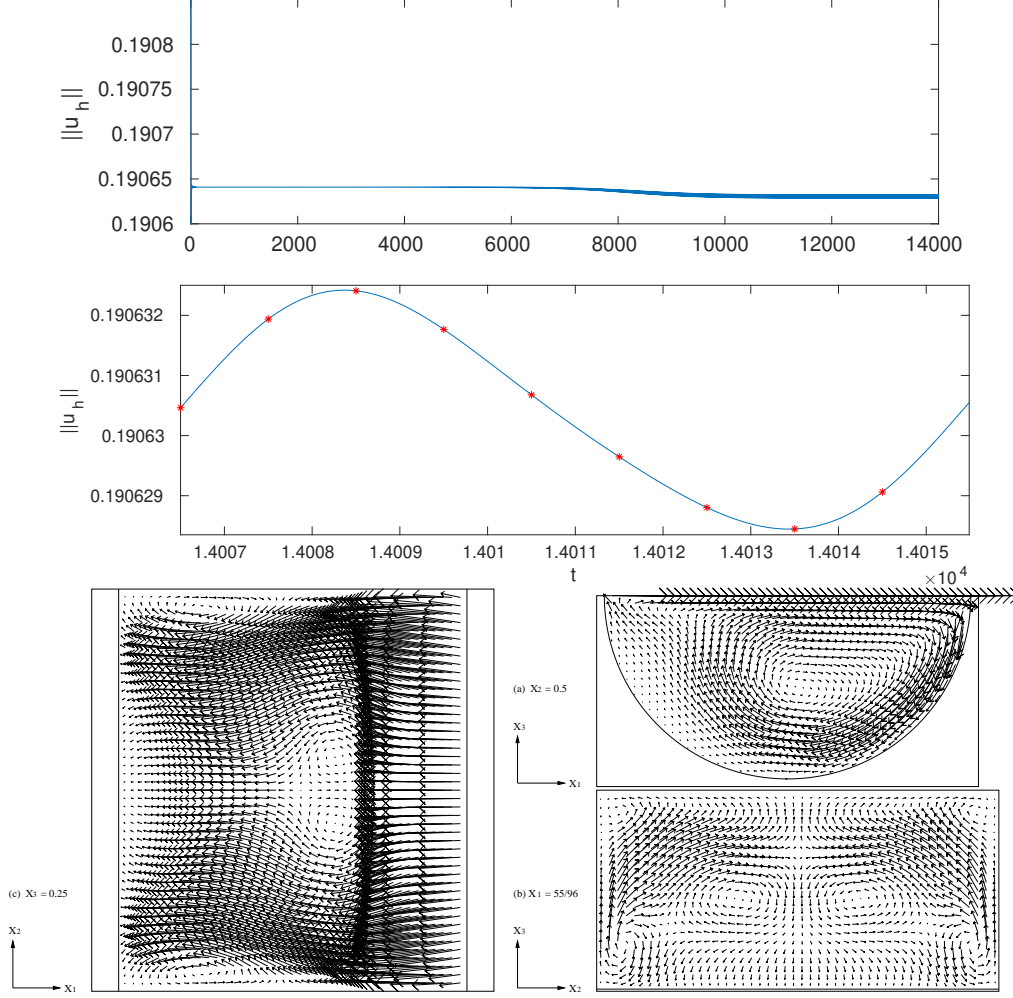


Figure 12: History of  $\|u_h\|$  (top) and that of one period (2nd one from top) in a semicircular cavity for  $Re = 930$ , averaged velocity field projected on planes:  $x_3 = 0.25$  (bottom left),  $x_2 = 0.5$  (middle right), and  $x_1 = 55/96$  (bottom right) for  $h = 1/96$  and  $\Delta t = 0.001$ . (In the bottom left and right plots, the vector scale is four times of the actual one to enhance visibility.)

(whose oscillating amplitude increases in time as shown in Figure 9). For  $Re=930$  and  $950$ , both histories of  $\|u_h\|$  do oscillate with fixed amplitudes, respectively (see Figures 12 and 13). The angular frequencies are  $0.7031317$  and  $0.6981317$  for  $Re=930$  and  $950$ , respectively. Their averaged velocity

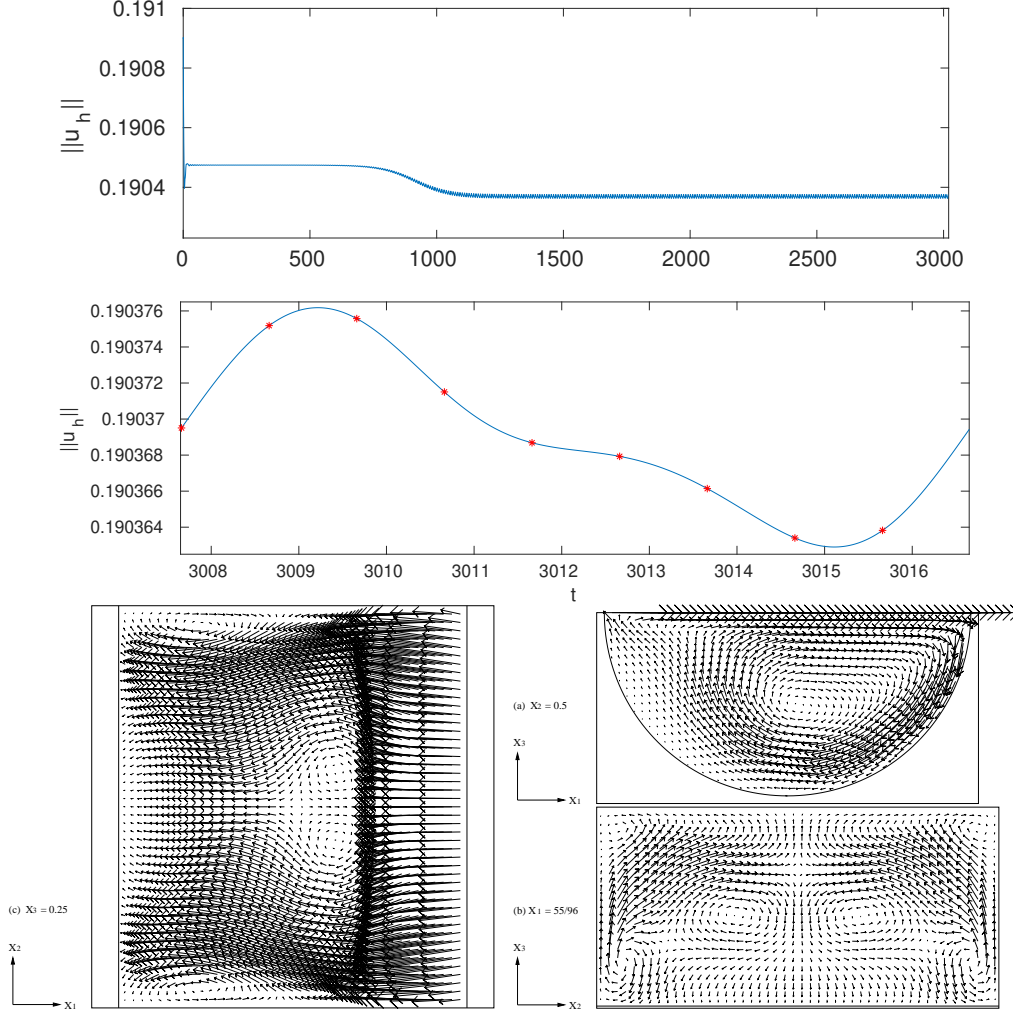


Figure 13: History of  $\|u_h\|$  (top) and that of one period (2nd one from top) in a semicircular cavity for  $Re = 950$ , averaged velocity field projected on planes:  $x_3 = 0.25$  (bottom left),  $x_2 = 0.5$  (middle right), and  $x_1 = 55/96$  (bottom right) for  $h = 1/96$  and  $\Delta t = 0.001$ . (In the bottom left and right plots, the vector scale is four times of the actual one to enhance visibility.)

plots in Figures 12 and 13 show very close similarity to those in Figure 10 for  $Re=927$ . To find out how oscillation mode evolves from  $Re=927$  to 950, we have compared the snapshots of oscillation mode for  $Re=930$  and 950



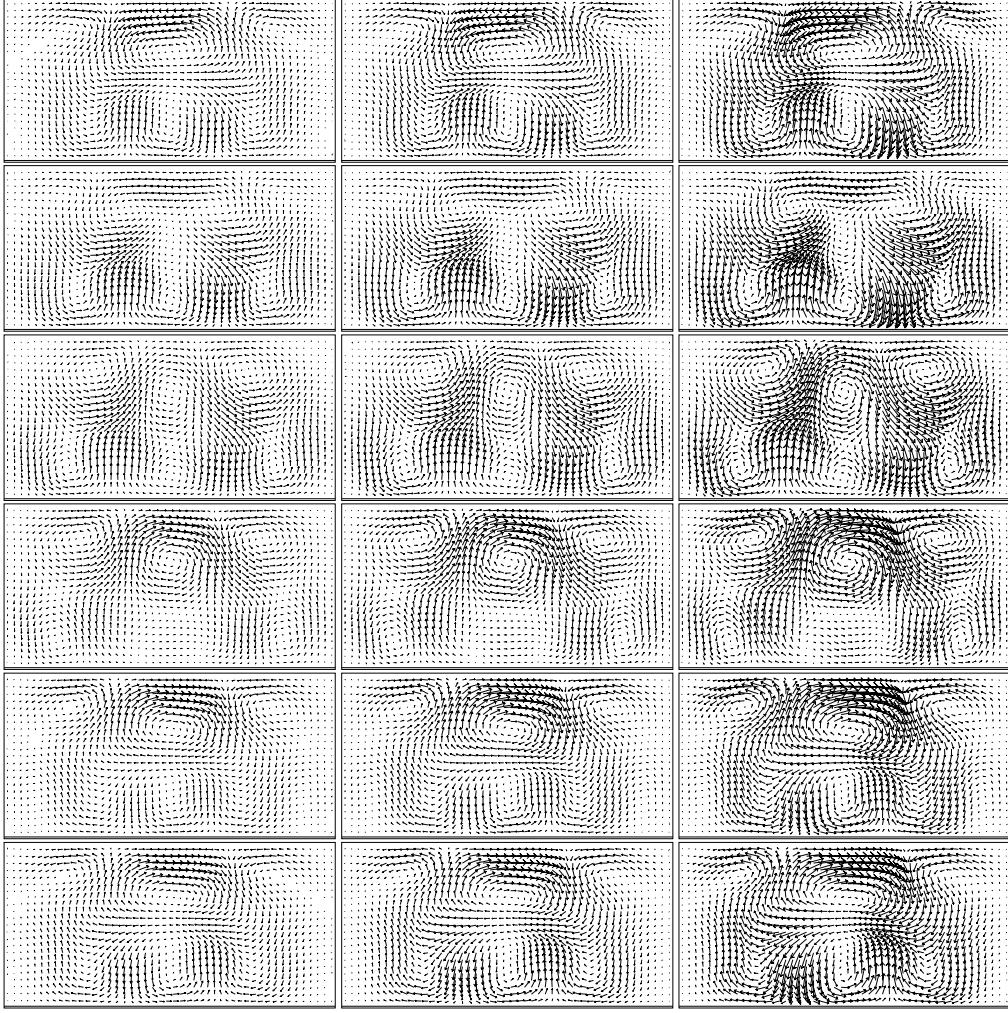


Figure 14: Oscillation mode projecting on plane  $x_1 = 55/96$  in a semicircular cavity for  $\text{Re}=927$  (left) at  $t = 15006, 15007, 15008, 15009, 15010$ , and  $15010.5$  (from top to bottom),  $\text{Re}=930$  (middle) at  $t = 14006.5, 14007.5, 14008.5, 14009.5, 14010.5$ , and  $14011$  (from top to bottom), and  $\text{Re}=950$  (right) at  $t = 3007.65, 3008.65, 3009.65, 3010.65, 3011.65$ , and  $3012.15$  (from top to bottom). Velocity vectors have been magnified to enhance visibility.

at several instances to those for  $\text{Re}=927$  as shown in Figures 14 and 15. It is interesting to find out that the oscillation mode is almost the same for

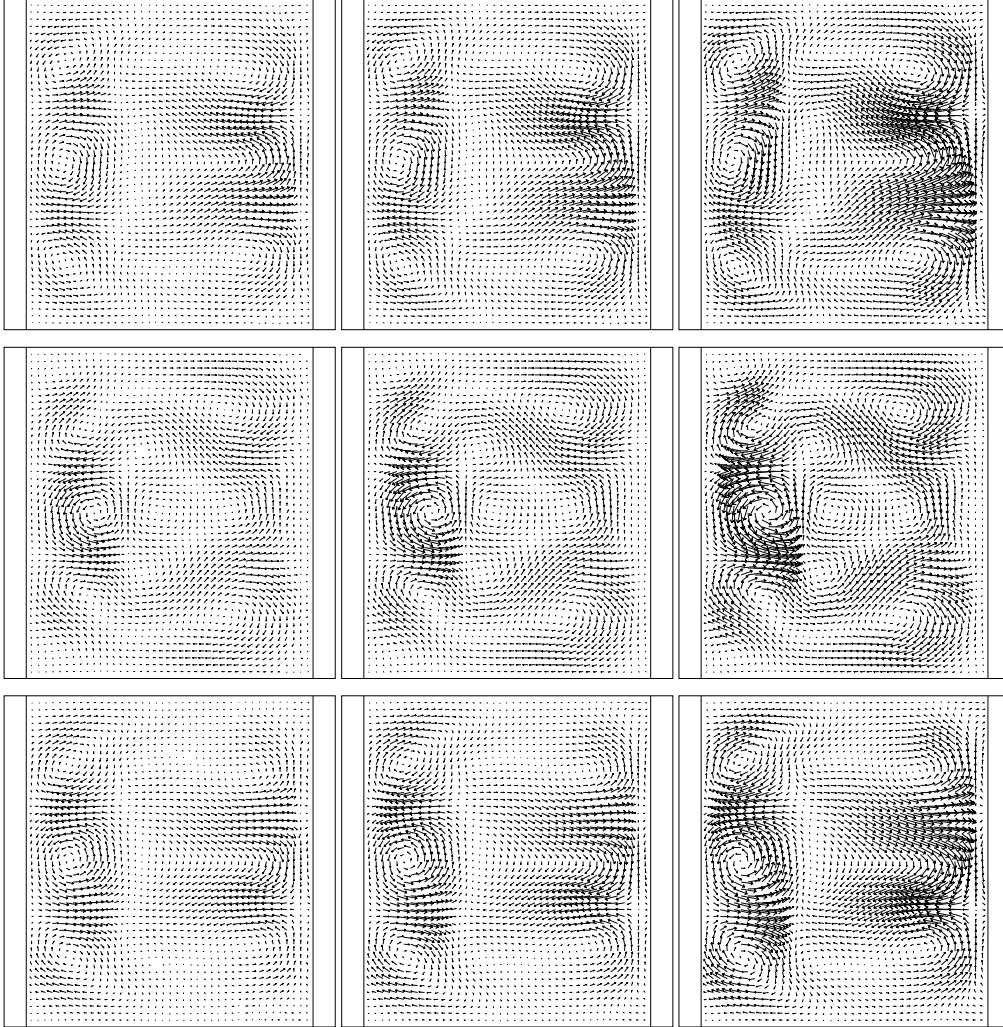


Figure 15: Oscillation velocity field (difference) projecting on plane  $x_3 = 0.25$  for  $\text{Re}=927$  (left) at  $t = 15006, 15008$ , and  $15010$  (from top to bottom),  $\text{Re}=930$  (middle) at  $t = 14006.5, 14008.5$ , and  $14010.5$  (from top to bottom), and  $\text{Re}=950$  (right) at  $t = 3007.65, 3009.65$ , and  $3011.65$  (from top to bottom). Velocity vectors have been magnified to enhance visibility.

those three Reynolds numbers. Those computational results for  $\text{Re}=927, 930$ , and  $950$  suggest that the oscillation mode in Figures 14 and 15 is the one associated with the Hopf bifurcation and originated at  $\text{Re}$  less than the

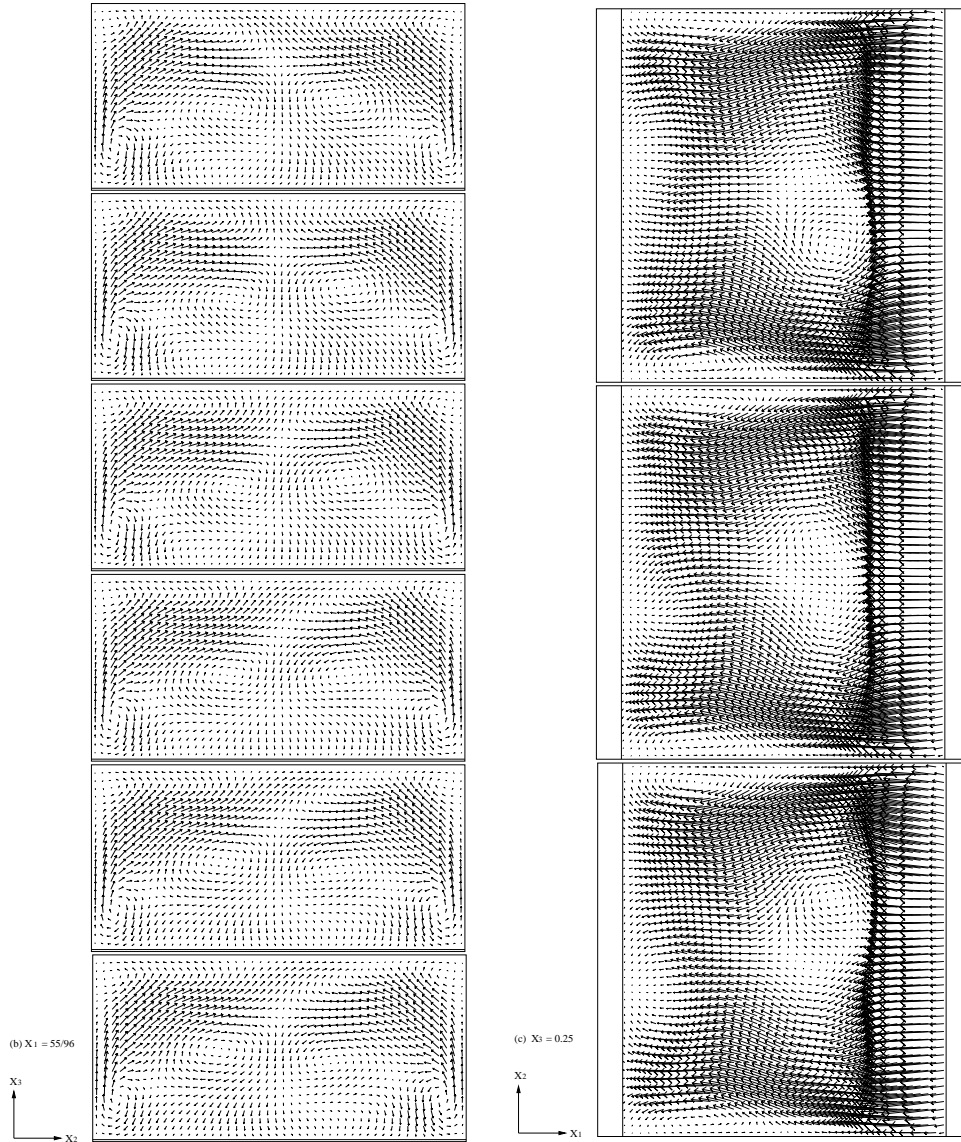


Figure 16: Velocity field projecting on the planes  $x_1 = 55/96$  (left six) at  $t = 3007.65, 3008.65, 3009.65, 3010.65, 3011.65,$  and  $3012.15$  (from top to bottom) and  $x_3 = 0.25$  (right three) at  $t = 3007.65, 3009.65,$  and  $3011.65$  (from top to bottom) for  $\text{Re}=950$ .

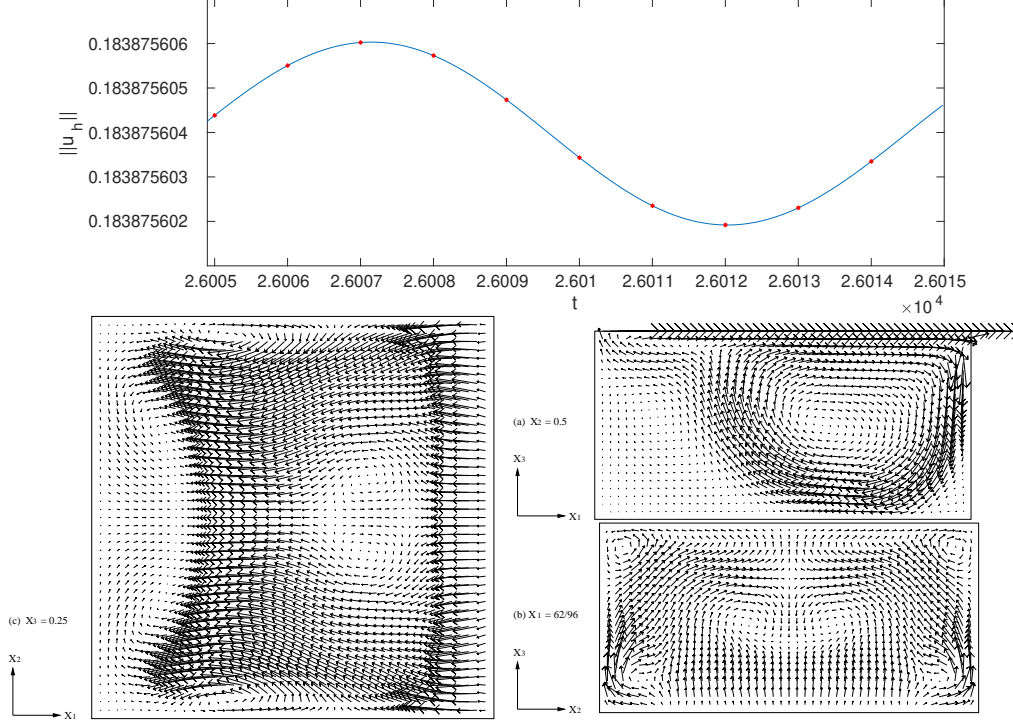


Figure 17: History of  $\|\mathbf{u}_h\|$  for one period in a shallow cavity with a unit square base for  $Re = 1364$  (top), averaged velocity field projected on planes:  $x_3 = 0.25$  (bottom left),  $x_2 = 0.5$  (middle right), and  $x_1 = 62/96$  (bottom right) for  $h = 1/96$  and  $\Delta t = 0.001$ . (In the bottom left and right plots, the vector scale is four times that of the actual one to enhance visibility.)

critical Reynolds number.

Since the oscillation amplitude of  $\|\mathbf{u}_h^n\|$  in a time period shown in Figure 10 is about the order of  $10^{-11}$  for  $Re=927$ , the change of velocity field from the average velocity field is very hardly to be observed. But for  $Re=950$ , the change of velocity field (due to the oscillation mode) can be observed in Figure 16 via the comparison to those in Figure 13. On plane  $x_1 = 55/96$  the size of vortices in the middle of those plots varies periodically and they oscillate slightly up and down. Similar on the plane  $x_3 = 0.25$ , the size of vortices in the middle of those plots varies periodically. Another observation is that the Taylor-Görtler-like vortices are not presented at the bottom of projected velocity field on the plane  $x_1 = 55/96$  in Figures 14 and 16 for this



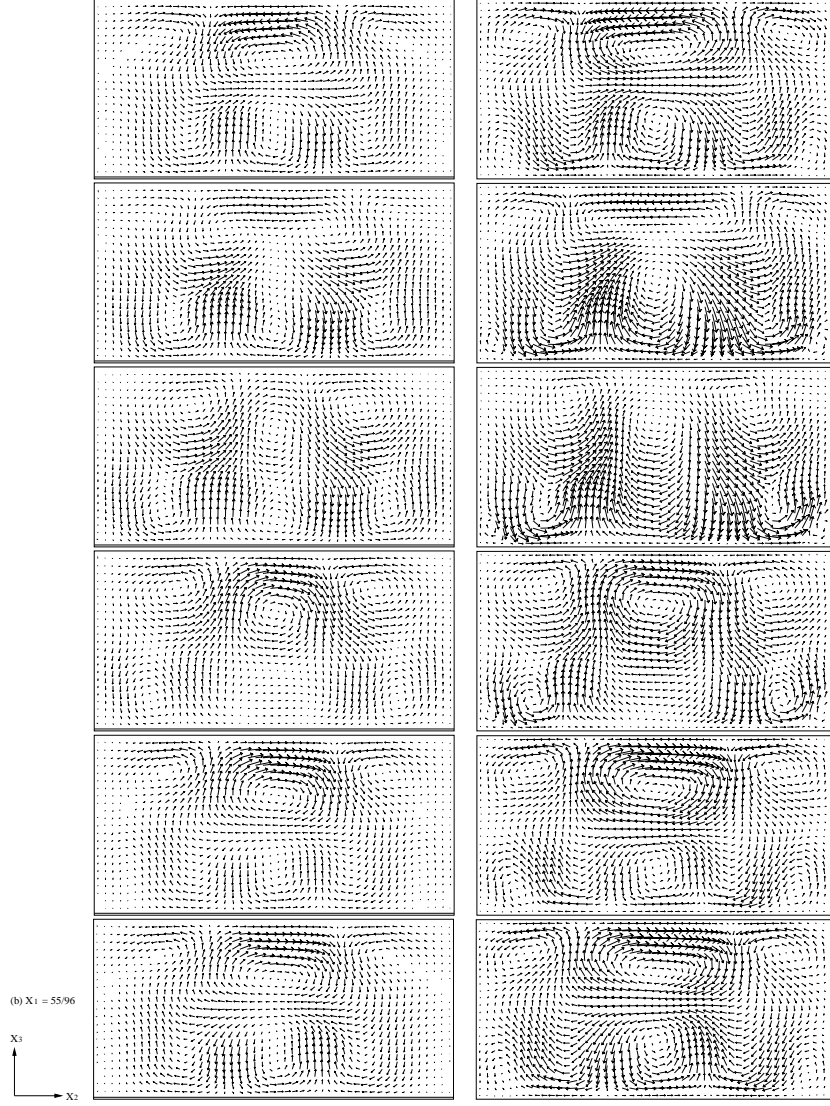


Figure 18: Oscillation mode projecting on plane (i)  $x_1 = 55/96$  for  $\text{Re}=927$  in a semicircular cavity (left) at  $t = 15006, 15007, 15008, 15009, 15010$ , and  $15010.5$  (from top to bottom) and (ii)  $x_1 = 62/96$  for  $\text{Re}=1364$  (right) in a shallow cavity at  $t = 26005, 26006.1, 26007.19, 26008.29, 26009.39$ , and  $26009.9$  (from top to bottom). Velocity vectors have been magnified to enhance visibility.

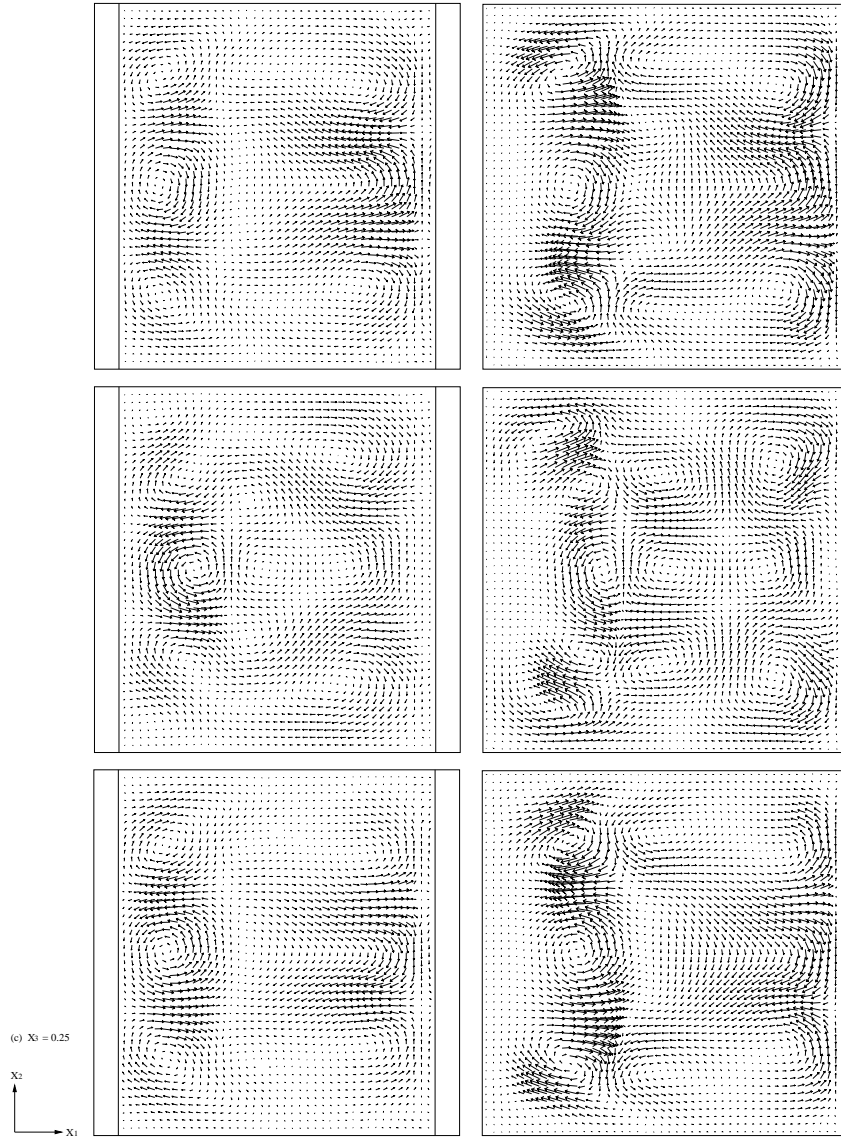


Figure 19: Oscillation velocity field (difference) projecting on plane  $x_3 = 0.25$  for  $\text{Re}=927$  (left) at  $t=15006$ ,  $15008$ , and  $15010$  (from top to bottom) and for  $\text{Re}=1364$  (right) in a shallow cavity at  $t = 26005$ ,  $26007.19$ , and  $26009.39$  (from top to bottom). Velocity vectors have been magnified to enhance visibility.

case.

To find out the effect of semicircular shape on lid-driven cavity flows, we have compared the above computational results at  $Re=927$  to those in a shallow cavity with a unit square flat bottom and height of  $1/2$ . As reported in [16], the critical Reynolds number for lid-driven flow in this shallow cavity is between 1364 and 1365 for the mesh size  $h = 1/96$  and time step  $\Delta t = 0.001$ . The averaged velocity field and one period of  $\|\mathbf{u}_h\|$  for  $Re=1364$  are shown in Figure 17. The averaged velocity field projected on  $x_2 = 0.5$  is quite different from the one in a semicircular cavity shown in Figure 10 due to the two different cross section shapes. But the similarity of averaged velocity field on the planes  $x_3 = 0.25$  and  $x_1 = 62/96$  in Figure 17 can be found from those on planes  $x_3 = 0.25$  and  $x_1 = 55/96$  shown in Figure 10. Snapshots of oscillation mode for  $Re=1364$  from the first half of a period are presented in Figures 18 and 19. Comparing to those of  $Re=927$  in a semicircular cavity (see Figures 18 and 19), we have found a very close similarity of the main flow circulation pattern. But in a shallow cavity, the main difference in Figure 18 is that small vortices always exist at two lower corners, which are triggered by the presence of two vertical side walls and downstream wall.

## 4 Conclusion

In this article, we have studied numerically the transition from steady flow to oscillatory one in a semicircular cavity of width and depth 1. Our simulation results show that the value of critical Reynolds number  $Re_{cr}$  for the transition from steady flow to oscillatory (a Hopf bifurcation) lie somewhere in the interval (927, 928) for  $h = 1/96$ . The oscillating angular frequency is between 0.70736 and 0.70345. The flow velocity oscillation at  $Re$  close to  $Re_{cr}$  has been investigated in detail. We have visualized how the oscillating mode evolves for different  $Re$  values. Numerical results indicate that the oscillation mode starts before  $Re=927$  is the one associated with the Hopf bifurcation at  $Re=930$  and 950. Concerning the effect of semicircular shape on lid-driven cavity flow, we have found that the oscillation mode in a semicircular cavity shows a close similarity to the one obtained in a shallow cavity, but with some difference triggered by the presence of two vertical side walls and downstream wall in a shallow cavity.



## References

- [1] Z. Feng and H. Lim, “Multi-relaxation time lattice Boltzmann simulations of oscillatory instability in lid-driven flows of 2D semi-elliptical cavity,” *J. Vis.* **22**, 1057-1070 (2019).
- [2] P. N. Shankar and M. D. Deshpande, “Fluid mechanics in the driven cavity,” *Annu. Rev. Fluid Mech.* **32**, 93-136 (2000).
- [3] J.-L. Guermond, C. Migeon, G. Pineau, and L. Quartapelle, “Start-up flows in a three-dimensional rectangular driven cavity of aspect ratio 1: 1: 2 at  $Re = 1000$ ,” *J. Fluid Mech.* **450**, 169-199 (2002).
- [4] H.C. Kuhlmann and F. Romanò, The Lid-Driven Cavity. In: Gelfgat, A. (eds) *Computational Modelling of Bifurcations and Instabilities in Fluid Dynamics. Computational Methods in Applied Sciences*, vol 50. Springer, Cham.
- [5] C. K. Aidun, N. G. Triantafillopoulos, and J. D. Benson, “Global stability of a lid-driven cavity with throughflow: Flow visualization studies,” *Phys. Fluids A* **3**, 2081-2091 (1991).
- [6] L. M. González, E. Ferrer, and H. R. Díaz-Ojeda, “Onset of three-dimensional flow instabilities in lid-driven circular cavities,” *Phys. Fluids* **29**, 064102 (2017).
- [7] J. Gerrits, *Fluid Flow in 3D Complex Geometries A Cartesian Grid Approach* Master thesis, University of Groningen, Groningen, Netherlands, 1996.
- [8] R. Glowinski and T.-W. Pan, *Numerical Simulation of Incompressible Viscous Flow: Methods and Applications* (De Gruyter, Berlin/Boston 2022).
- [9] Z. Belhachmi, C. Bernardi, and A. Karageorghis, “Spectral element discretization of the circular driven cavity. part iv: The Navier–Stokes equations,” *J. Math. Fluid Mech.* **6**, 121-156 (2004).
- [10] R. Glowinski, G. Guidoboni, and T.-W. Pan, “Wall-driven incompressible viscous flow in a two-dimensional semi-circular cavity,” *J. Comput. Phys.* **216**, 76–91 (2006).

- [11] C. Migeon, A. Texier, and G. Pineau, “Effects of lid-driven cavity shape on the flow establishment phase,” *J. Fluids Struct.* **14**, 469-488 (2000).
- [12] R. Iwatsu, J. M. Hyun, and K. Kuwahara, “Analyses of three-dimensional flow calculations in a driven cavity,” *Fluid Dyn. Res.* **6**, 91-102 (1990).
- [13] F. Giannetti, P. Luchini, and L. Marino, “Linear stability analysis of three-dimensional lid-driven cavity flow,” in *Atti del XIX Congresso AIMETA di Meccanica Teorica e Applicata* (Aras Edizioni Ancona, Italy, 2009), pp. 738.1-718.10.
- [14] Y. Feldman and A. Y. Gelfgat, “Oscillatory instability of a three-dimensional lid-driven flow in a cube,” *Phys. Fluids* **22**, 093602 (2010).
- [15] A. Liberzon, Y. Feldman, and A. Y. Gelfgat, “Experimental observation of the steady-oscillatory transition in a cubic lid-driven cavity,” *Phys. Fluids* **23**, 084106 (2011).
- [16] T.-W. Pan, S.-H. Chiu, A. Guo, and J. He, “Numerical study of transitions in lid-driven flows in shallow cavities,” *Comptes Rendus. Mécanique* **351**, 1-17 (2023).
- [17] *Splitting methods in communication, imaging, science, and engineering* edited by R. Glowinski, S.J. Osher and W. Yin (Springer, 2016).
- [18] T. Wang, T.-W. Pan, and R. Glowinski, “A comparison of  $L^2$ -projection and  $H^1$ -projection methods for the numerical simulation of incompressible viscous fluid flow: A case study,” *Chinese Journal of Engineering Mathematics* **25**, 761-778 (2008).
- [19] T.-W. Pan and R. Glowinski, “A projection/wave-like equation method for the numerical simulation of incompressible viscous fluid flow modeled by the Navier-Stokes equations,” *Computational Fluid Dynamics Journal* **9**, 28-42 (2009).
- [20] R. Glowinski, T.-W. Pan, T. I. Hesla, and D. D. Joseph, “A distributed Lagrange multiplier/fictitious domain method for particulate flows,” *Int. J. Multiphase Flow* **25**, 755-794 (1999).

- [21] R. Glowinski, T.-W. Pan, T. I. Hesla, D. D. Joseph, and J. Périaux, “A fictitious domain approach to the direct numerical simulation of incompressible viscous flow past moving rigid bodies: Application to particulate flow,” *J. Comput. Phys.* **169**, 363-426 (2001).
- [22] T.-W. Pan and S.-H. Chiu, “A DLM/FD method for simulating balls settling in Oldroyd-B viscoelastic fluids,” *J. Comp. Phys.* **484**, 112071 (2023).
- [23] R. Glowinski, “Finite element methods for incompressible viscous flow,” in *Handbook of Numerical Analysis*, edited by P. G. Ciarlet and J.-L. Lions (North-Holland, Amsterdam, 2003), Vol. IX, pp. 3-1176.
- [24] M. O. Bristeau, R. Glowinski, and J. Périaux, “Numerical methods for the Navier-Stokes equations. Applications to the simulation of compressible and incompressible viscous flow,” *Computer Physics Reports* **6**, 73-187 (1987).
- [25] E.J. Dean and R. Glowinski, “A wave equation approach to the numerical solution of the Navier-Stokes equations for incompressible viscous flow,” *C.R. Acad. Sci. Paris, Série I*, t. **325**, 783-791 (1997).
- [26] E. Dean, R. Glowinski, and T.-W. Pan, “A wave equation approach to the numerical simulation of incompressible viscous fluid flow modeled by the Navier-Stokes equations,” in *Mathematical and numerical aspects of wave propagation*, edited by J. De Santo (SIAM, Philadelphia, 1998), pp. 65-74.
- [27] H. C. Kuhlmann and S. Albensoeder, “Stability of the steady three-dimensional lid-driven flow in a cube and the supercritical flow dynamics,” *Phys. Fluids* **26**, 024104 (2014).

